Chinese Chemical Letters 36 (2025) 109935

Contents lists available at ScienceDirect

Chinese Chemical Letters

journal homepage: www.elsevier.com/locate/cclet

Electronic modulation of VN on $Co_{5.47}N$ as tri-functional electrocatalyst for constructing zinc-air battery to drive water splitting

Xinxin Zhang, Zhijian Liang, Xu Zhang, Qian Guo, Ying Xie*, Lei Wang*, Honggang Fu*

Key Laboratory of Functional Inorganic Material Chemistry, Ministry of Education of the People's Republic of China, Heilongjiang University, Harbin 150080, China

ARTICLE INFO

Article history:
Received 6 March 2024
Revised 2 April 2024
Accepted 28 April 2024
Available online 29 April 2024

Keywords:
Tri-functional activity
Electronic compensation effect
Heterojunction
Zinc-air batteries
Water splitting

ABSTRACT

Developing effective strategy for constructing the electrocatalysts enable tri-functional electrocatalytic activity of hydrogen evolution reaction (HER), oxygen evolution reaction (OER) and oxygen reduction reaction (ORR) is the premise to achieve both the zinc-air battery (ZAB) and overall water splitting. Herein, we utilize density functional theory to calculate the cobalt nitride (Co_xN, $x = 1$, 2, 4, 5.47) system, revealing that the $Co_{5.47}N$ maybe exhibits a tri-functional activity due to the diverse valence states and high-density d-electron state of Co site. Furthermore, the electron of Co site is further delocalized by the electronic compensation effect of vanadium nitride (VN), thus improving the intermediates absorption and electrocatalytic activity. Accordingly, the $Co_{5.47}N$/VN heterojunction is designed and synthesized *via* an electrospinning and a subsequent pyrolysis route. As expected, it displays excellent HER, OER, and ORR activity in alkaline electrolyte, which can be applied to assemble ZAB with a high power density of 207 mW/cm^2 and overall water splitting system only requires a lower voltage of 1.53 V to achieve 10 mA/cm^2. The electron regulation effect of VN makes the Co valence state decrease in the reduction reaction whereas increase in the oxidization reaction as evidenced by quasi-operando XPS analyses. Importantly, two ZABs connected in series could drive overall water splitting, indicating the potential application in renewable energy technologies.

The renewable energy technology, such as metal-air batteries and water splitting devices, has been recognized as a critical approach in tackling the ongoing energy crisis and environmental challenges [1,2]. Hydrogen evolution reaction (HER), oxygen evolution reaction (OER), and oxygen reduction reaction (ORR) are the crucial reactions for zinc-air battery (ZAB) and water splitting devices [3-5]. Nevertheless, these reactions are relatively sluggish kinetics since multiple electron transfer step, which consistently require large overpotential [6,7]. Nowadays, Pt-based and Ir/Ru-based electrocatalysts have been considered as the benchmark catalysts for HER/ORR and OER, respectively, but their single catalytic activity, instability, and high cost impede widespread applications [8-10]. Since the cathode and anode of energy devices are often influenced by the electrolyte composition, applied potential window and *etc*., utilizing diverse catalysts for the two electrodes will increase the complexity and cost, maybe induce side reactions on the catalyst surface [11]. Therefore, developing non-precious metal-based catalysts with multifunctional activity is essential for addressing the above issues [12-14]. Because the intermediates of different reactions show diverse properties, so the requirements for catalytic active sites are different. It is difficult for a single catalytic active site to exhibit both high oxidation and reduction activity at the same time. Generally, electrons tend to easily escape more from low work-function (WF) surfaces and transfer to intermediate species (H*, OOH*, O*, and OH*), thus benefiting to reduce the electron transfer resistance at the solid-liquid interface. It had been reported that the lower oxidation state metal active centers could enhance the HER and ORR activities due to the shift of d-band centers towards lower energies [15-22]. Conversely, the surfaces with higher WF tend to act as electron acceptors, which facilitates the transfer of electrons from adsorbed species to the catalyst surface. The d-band centers of most high-valence metals approach the Fermi level (E_f), thereby enhancing the bond strength between intermediates and surface sites to improve the OER activity [23-26]. In view of this, the key to exploring tri-functional catalysts is to resolve the competition active sites for oxidation and reduction reactions.

Transition metal interstitial nitrides (TMINs) have unique electronic structure and exhibit Pt-like property [27,28]. TMINs with tunable chemical compositions that can effectively modulate

* Corresponding authors.
E-mail addresses: xieying@hlju.edu.cn (Y. Xie), wanglei0525@hlju.edu.cn (L. Wang), fuhg@vip.sina.cn, fuhg@hlju.edu.cn (H. Fu).

https://doi.org/10.1016/j.cclet.2024.109935
1001-8417/

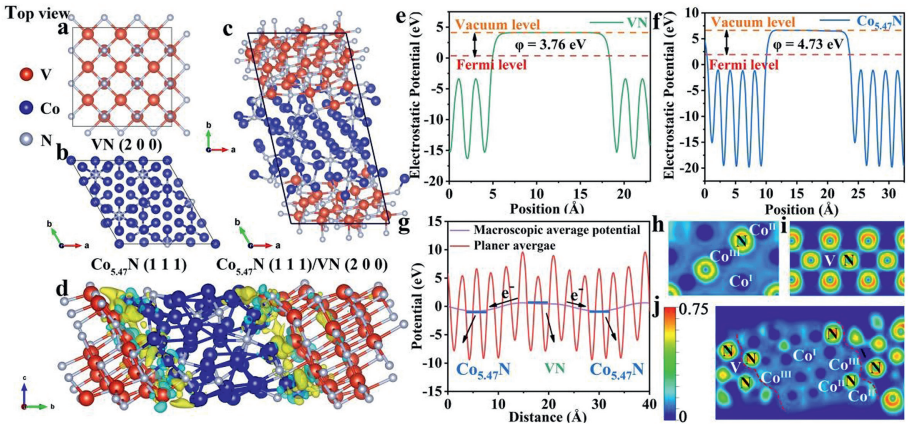

Fig. 1. (a–c) The theoretical models of $Co_{5.47}N$ (111), VN (200) and $Co_{5.47}N$/VN. (d) EDD diagram of $Co_{5.47}N$/VN, where yellow and blue regions represent electron accumulation and depletion area, respectively. WF of (e) VN and (f) $Co_{5.47}N$. (g) The macroscopic average potential of $Co_{5.47}N$/VN. ELF diagrams of (h) $Co_{5.47}N$, (i) VN, and (j) $Co_{5.47}N$/VN.

the d-band centers of metal atoms for enhancing the adsorption/desorption ability of intermediate [26,29-45]. Relatively, Co_xN ($x = 1$, 2, 4, 5.47) possesses various stoichiometries lead to diverse oxidation states of Co species, indicating that broad applications in HER, ORR and OER [30,46]. The high oxidation state of Co in Co_xN with low Co content is favorable for OER performance, while the low oxidation state of Co in Co_xN with high Co content shows excellent HER and ORR activity [32-39]. The reported self-supported porous CoN@NC nanosheets exhibit tri-functional catalytic activities, but ORR activity is unideal with a high-potential of 0.77 V [40]. In the Co_2N@NC system with dual oxidation states (+2 and +3) of cobalt shows a much higher ORR activity (half-wave potential ($E_{1/2}$) = 0.84 V) [32]. Furthermore, the $E_{1/2}$ for Co_4N@CNNT catalyst is reported to be 0.86 V [42]. As the increase of Co content, the $E_{1/2}$ for $Co_{5.47}N$/RGO is up to ~0.94 V [44]. It can be concluded that the ORR activity of Co_xN can be promoted with the decrease of Co contents, the similar trend is discovered for the reduction reaction of HER [33,44,45]. The increase of Co content results in a reduction of electron density between Co and N, thereby enhancing the electron delocalization and conductivity of Co_xN and improving the reduction reaction electrocatalytic activity [38]. Due to the mutual restriction between oxidation and reduction reactions, it is necessary to construct heterojunction for further enhancing the tri-functional electrocatalytic activity of Co_xN [47]. Vanadium (V) is early transition metal with partially filled of d orbitals [48], and the introduction of vanadium nitride (VN) into Co_xN to construct heterojunction can utilize the electron compensation effect [49]. Meanwhile, it can cause the changes of the interface geometry and electronic structure, thus inducing the change of the natural electric field and coordination environment. The charge transfer behavior will intensify the change and diversity of valence states of the active sites on the interface, benefiting to improve of the tri-functional electrocatalytic activity.

Herein, density functional theory (DFT) calculations are used to reveal the effect of diverse valence states and high-density d-electron of Co_xN ($x = 1$, 2, 4, 5.47) on tri-functional electrocatalytic activity. Specially, the introduction of VN can regulate the electronic structure of $Co_{5.47}N$, thus altering the electrophilic/nucleophilic characteristics of Co sites and improving the adsorption and electrocatalytic activity of intermediates. Based on the above insight, $Co_{5.47}N$/VN particles embedded in nitrogen-doped carbon nanofibers ($Co_{5.47}N$/VN@NCFs) catalyst has been synthesized through electrospinning combined with thermal treatment strategy. It exhibits outstanding HER, OER and ORR electrocatalytic activity, while two series-connected ZABs could drive overall water splitting. *Quasi*-operando XPS demonstrates that VN can modulate the valence state of Co, decreasing during the reduction process and increasing during the oxidation process. Our study provides unique insights into the design and optimization of tri-functional electrocatalysts from the perspective of adjusting crystal stoichiometry and interface structure.

To elucidate the influence of compositional and structural changes on the electronic structures of Co_xN ($x = 1$, 2, 4, and 5.47), the density of states (DOSs) for Co_xN surfaces and the Bader charges for Co_xN bulk crystals were calculated. As depicted in Fig. S1 (Supporting information), the surface DOSs near the E_f for $Co_{5.47}N$ are higher than other Co_xN ($x = 1$, 2 and 4) catalysts, indicating its good electronic conductivity. The Bader charge analysis of the bulk phase (Table S1 in Supporting information) further confirms that the monovalent state of Co (0.887) in CoN is the highest among all considered Co_xN. With gradual increase of Co content, the Bader charge of Co decreases to 0.555 for Co_2N and further splits into 0.313 and 0.173 for Co_4N. Especially in $Co_{5.47}N$, Co exhibits three distinct oxidation states (0.102, 0.144, and 0.270). The Co catalytic sites with multi-valence nature are expected to play different roles during the HER, OER, and ORR and finally synergistically affect its overall electrocatalytic activities, which should be an important characteristic for multifunctional electrocatalysis. Beside the stoichiometry of the catalyst, the formation of heterojunction not only leads to changes in the interfacial coordination environment but also induces charge transfer between the two phases, resulting in the appearance of an internal built-in electric field at the interface. These factors will intensify the diversity and the oxidation state of the active sites significantly, altering their d-band center and the adsorption/desorption characteristics with intermediates and thus contributing to the multi-functional electrocatalytic activities of the catalysts. Figs. 1a–c show the optimized geometries of VN, $Co_{5.47}N$, and $Co_{5.47}N$/VN catalysts. The VN (200) and $Co_{5.47}N$ (111) surfaces have good lattice matching ($u = 7\%$, $v = 0.1\%$), and their interfacial binding energy is –1.491 eV/Å^2. This implies that the $Co_{5.47}N$/VN heterostructure possesses excellent interfacial stability, which is beneficial for maintaining the structural integrity of the catalyst during the catalytic process and thus its cyclic stability. The electron density difference (EDD) in Fig. 1d illustrates a redistribution of spatial charge density due to the alteration of interfacial coordination environment, confirming an electron transfer from VN to $Co_{5.47}N$. Moreover, the computed WF in Figs. 1e and f reveal a lower WF value for VN (3.76 eV) compared to $Co_{5.47}N$ (4.73 eV), and the macroscopic average electrostatic potential in the bulk VN region (0.72) is also higher than that of $Co_{5.47}N$ (–0.94) in Fig. 1g. Hence, the electron transfer from VN to $Co_{5.47}N$ induces an inherent electric field at the interface. This result is further sub-

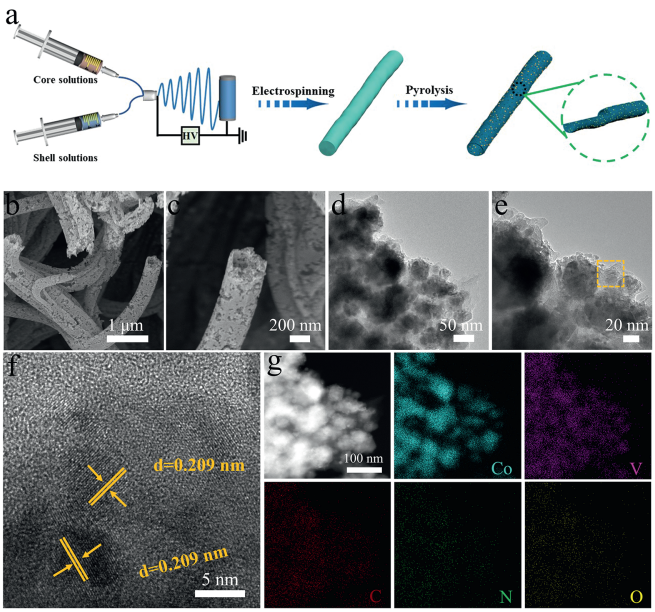

Fig. 2. (a) Schematic illustration for the synthesis of $Co_{5.47}N$/VN@NCFs. (b, c) SEM, (d) TEM, (e, f) HRTEM and (g) element mapping images of Co, V, C, N, and O for $Co_{5.47}N$/VN@NCFs.

stantiated by the Bader charge analysis. Relative to pristine VN surface, the average electron lost for V sites is ~0.05, while $Co_{5.47}N$ gained 0.16 electrons (Table S2 in Supporting information). In addition, the Bader charges for Co and V sites near the interface both exhibit obvious changes with respect to those in pristine VN and $Co_{5.47}N$ surfaces. The induced changes in oxidation states of the metal sites will result in their different bonding with the intermediates and thus affect the electrocatalytic mechanisms, which will be discussed in detail below. The electron localization function (ELF) can be used to analyze the electronic characteristics of active sites. In $Co_{5.47}N$ surface, three different coordination environments for Co atoms are considered, namely isolated CoI, CoII coordinated with individual N atoms, and CoIII coordinated with two N atoms. Around CoI and CoII, the electron density is relatively more delocalized compared to CoIII (Fig. 1h and Fig. S2 in Supporting information). The electron density distribution near the V sites in VN also exhibits notable delocalization characteristics. Conversely, the electron density distribution near the N sites in both VN and $Co_{5.47}N$ displays strong localization. Upon the formation of the $Co_{5.47}N$/VN heterojunction, the changes in coordination environments result in obviously diverse ELF distributions near the metal sites at the interface. The electron density around CoI, CoII, CoIII, and V at the interface shows higher delocalization compared to the $Co_{5.47}N$ and VN surfaces. Additionally, the ELF values near the N atoms at the interface experience significant reduction in Figs. 1i and j. The enhanced electron density delocalization near the active sites is beneficial for the adsorption and activation of intermediate species, as well as for facilitating charge transfer between them. This is advantageous for reducing charge transfer resistance at the solid-liquid interface and enhancing the activity of the reaction.

Based on theoretical analyses, $Co_{5.47}N$/VN@NCFs catalysts with hollow and mesoporous structures were synthesized *via* continuous coaxial electrospinning followed by ammonia (NH_3) treatment (Fig. 2a). Briefly, polyacrylonitrile (PAN), cobalt(II) acetate tetrahydrate ($Co(CH_3COO)_2{\cdot}4H_2O$), vanadium(III) chloride (VCl_3), 1,10-phenanthroline (*o*-phen), and polyvinylpyrrolidone (PVP) were dissolved in *N*,*N*-dimethylformamide (DMF) as precursor solutions for the shell layer. Concurrently, poly(methyl methacrylate) (PMMA) was dissolved in DMF to form precursor solutions for the core. Upon increasing the pyrolysis temperature, the PMMA encapsulated within the inner shell layer evaporated, resulting in the formation of hollow nanofibers. Simultaneously, the PVP and metal salts in the shell layer decomposed to develop mesopores/micropores and $Co_{5.47}N$/VN particles, respectively. It is notable that such a hollow structure can provide abundant contact interfaces between the electrode and electrolyte while simultaneously shortening the ion diffusion path, thereby promoting rapid electrochemical kinetics. Furthermore, the extensive hollow space facilitates the storage of a considerable charge, contributing to exceptional cycling performance. The scanning electron microscopy (SEM) (Fig. 2b) showed that the as-prepared electrocatalysts consist of carbon fibers with a distinctively hollow structure extending several micrometers in length. The high-magnification SEM (Fig. 2c) indicated the diameter of individual hollow fibers is approximately 350 nm. Additionally, the presence of the punching agent PVP and the etching effect of ammonia gas significantly contribute to the formation of substantial pores on the surface of fibers. For comparison, $Co_{5.47}N$@NCFs and VN@NCFs electrocatalysts were also prepared through controlled addition of metal salts, revealing variations in their morphology (Figs. S3a-d in Supporting information). These variations could be attributed to the potential impact of different metal additions on the shape, size, and pore structure of the fibers, thereby influencing the final appearance and properties of the nanofibers. Transmission electron microscopy (TEM) images of $Co_{5.47}N$/VN@NCFs in Figs. 2d and e further confirm the uniform distribution of particles with diameters of about 5–10 nm. The carbon fibers exhibit abundant mesopores and micropores, contributing to a larger surface area that facilitates the immobilization of more active sites (Figs. S4a and b in Supporting information). The high-resolution TEM (HRTEM) image in Fig. 2f reveals distinct lattice fringes with interplanar distance of 0.209 nm, corresponding to the (111) facet of $Co_{5.47}N$ and the (200) facet of VN. Furthermore, Co, V, C, N, and O elements are evenly distributed in whole area of $Co_{5.47}N$/VN@NCFs from scanning TEM (STEM) image and energy-dispersive X-ray spectroscopy (EDS) elemental mapping (Fig. 2g).

The X-ray diffraction (XRD) characterization was employed to identify the phases of electrocatalysts. As displayed in Fig. 3a, the characteristic peaks observed at 37.6°, 43.7°, 63.5°, 76.2°, and 80.3° can be attributed to the (111), (200), (220), (311), and (222) planes of cubic VN (PDF#35-0768) [50]. Simultaneously, the characteristic peaks at 43.7°, 50.9°, and 74.9° correspond to the (111), (200), and (220) lattice planes of $Co_{5.47}N$ (PDF#41-0943) [51,52]. These results demonstrate that $Co_{5.47}N$ and VN are successfully integrated, primarily formed from the reduced products of metal ions and *o*-phen. Additionally, the XRD peak at 21.5° is associated with the amorphous carbon in the carbon nanofibers, implying the possible presence of defects on the carbon nanofibers. For comparison, the diffraction peaks and morphology of N-PVP and N-*o*-phen were obtained without the addition of PVP and *o*-phen, respectively, revealing the absence of lavish vacant pores on the surface, as displayed in Figs. S5 and S6 (Supporting information). Raman spectra in Fig. 3b exhibit two distinct peaks of $Co_{5.47}N$@NCFs (1353.1 and 1590.4 cm^{-1}) and VN@NCFs (1355.3 and 1590.4 cm^{-1}), which are assigned to disordered carbon (defect D band) and sp^2–hybridized carbon (graphitic G band), respectively [53,54]. However, the D and G peaks of $Co_{5.47}N$/VN@NCFs slightly shift towards higher wavenumbers (1359.7 and 1601.16 cm^{-1}), demonstrating that the charge density has changed after VN introduced. The I_D/I_G ratio of $Co_{5.47}N$/VN@NCFs is 0.91, which is higher than those of $Co_{5.47}N$@NCFs (0.84) and VN@NCFs (0.90), implying the higher defective degree of $Co_{5.47}N$/VN@NCFs. The abundant defects help to enhance the stability of the catalyst, while the highly activity in the defect region facilitates interac-

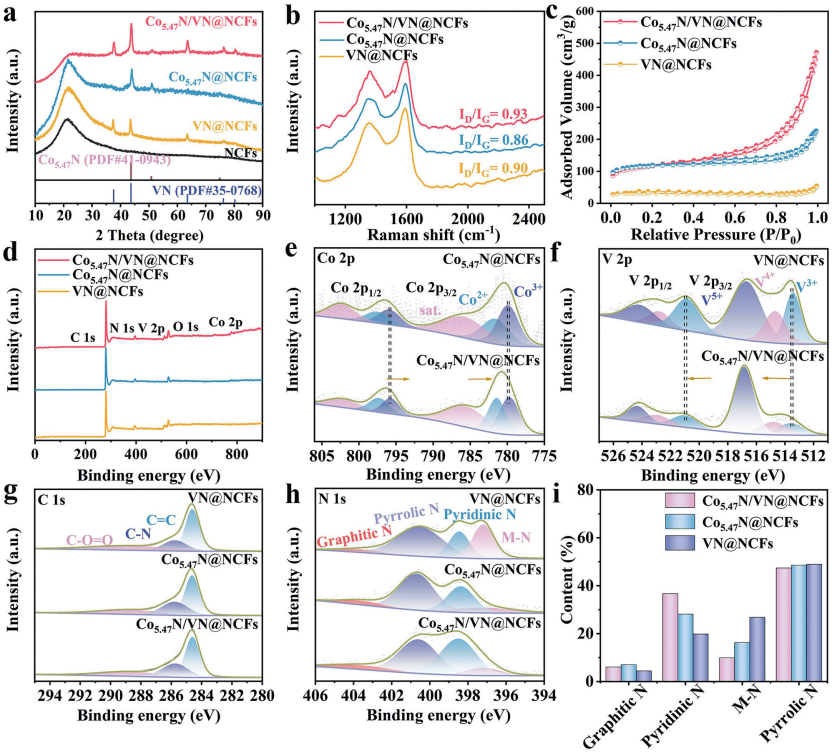

Fig. 3. (a) XRD patterns, (b) Raman spectra and (c) N_2 adsorption-desorption isotherms of $Co_{5.47}N$/VN@NCFs, $Co_{5.47}N$@NCFs and VN@NCFs. (d) Wide spectra, and high-resolution XPS spectra of (e) Co 2p, (f) V 2p, (g) C 1s, (h) N 1s and (i) the corresponding N-species content distribution.

tion with the precursor, resulting in a uniform growth of the catalyst on the surface of the NCFs, reflecting its confinement effect. The Brumauer-Emmett-Teller (BET) surface areas of as–prepared $Co_{5.47}N$/VN@NCFs, $Co_{5.47}N$@NCFs, VN@NCFs, N-*o*-phen@NCFs, and N-PVP@NCFs are measured to be 391.25, 381.60, 95.13, 336.68, and 329.73 m^2/g, respectively (Fig. 3c and Fig. S7 in Supporting information). Especially, $Co_{5.47}N$/VN@NCFs also possesses a considerable pore volume (0.73 cm^3/g) and pore diameter (7.46 nm) (Table S3 in Supporting information). Thus the incorporation of VN significantly increases the surface area and hollow porous structure of $Co_{5.47}N$@NCFs, leading to the exposure of abundant active sites and efficient mass transfer in $Co_{5.47}N$/VN@NCFs.

To precisely elucidate the impact of VN on the chemical composition and relevant chemical states of $Co_{5.47}N$@NCFs, X-ray photoelectron spectroscopy (XPS) analysis was carried out. Evident in the wide scan survey of $Co_{5.47}N$/VN@NCFs is the presence of elements Co, V, N, and C, along with absorbed O with contents of Co, V, N, and C at 1.1, 1.4, 4.9, and 92.6 at%, respectively (Fig. 3d and Table S4 in Supporting information). The high-resolution Co 2p region of $Co_{5.47}N$/VN@NCFs, XPS signal fitting revealed the presence of two oxidation states of Co elements, Co^{3+} at 779.7 and 795.7 and Co^{2+} at 781.4 and 797.3 eV [55,56]. For $Co_{5.47}N$@NCFs, the binding energy at 779.9 and 795.9 eV is assigned as Co^{3+}, and the binding energy at 781.6 and 797.5 eV corresponds to Co^{2+} (Fig. 3e). In the V 2p spectrum of $Co_{5.47}N$/VN@NCFs can fit three pairs of peaks, 513.5/521.1 eV, 514.8/522.9 eV, and 517.0/524.3 eV, belonging to V^{3+}, V^{4+}, and V^{5+} species, respectively (Fig. 3f) [57,58]. For VN@NCFs, the three pairs of peaks are located at 513.3/520.9 eV, 514.6/522.7 eV, and 516.8/524.1 eV, respectively. Interestingly, $Co_{5.47}N$/VN@NCFs exhibits a positive shift of 0.2 eV relative to V $2p_{1/2}$ and V $2p_{3/2}$ of the VN@NCFs, whereas $Co_{5.47}N$/VN@NCFs exhibits a negative shift of 0.2 eV from Co $2p_{1/2}$ and Co $2p_{3/2}$ compared to $Co_{5.47}N$@NCFs. The strong electronic interactions are confirmed on the $Co_{5.47}N$/VN, where the charge transfer occurs from the VN portion to the $Co_{5.47}N$. This result is in good agreement with the EDD and WF analyses. Figs. 3g and h show no significant changes in the binding energies of the C 1s and N 1s for the VN@NCFs, the $Co_{5.47}N$@NCFs, and the $Co_{5.47}N$/VN@NCFs. The C 1s of $Co_{5.47}N$/VN@NCFs were deconvoluted into C=C (284.6 eV), C–N (285.7 eV), and C–C=O (289.1 eV) [59]. The presence of C–N indicates that the element N was successfully doped into the carbon fibers backbone. The peaks of N 1s spectrum were fitted to metal-nitrogen (397.2 eV), pyridine nitrogen (398.4 eV), pyrrole nitrogen (400.6 eV), and graphite nitrogen (403.6 eV) with content of 9.91%, 36.67%, 47.37%, and 6.05%, respectively [60,61]. Among them, pyridine nitrogen, pyrrole nitrogen, and graphite nitrogen can significantly enhance the electrocatalytic activity sites and electron conductivity of the catalysts (Fig. 3i).

The electrocatalytic activity of $Co_{5.47}N$/VN@NCFs is pivotal for the HER as it constitutes an important half-reaction in overall water splitting systems. As shown in Fig. 4a and Fig. S8 (Supporting information), $Co_{5.47}N$/VN@NCFs exhibited s lower overpotential of 89 mV compared to $Co_{5.47}N$@NCFs (151 mV), VN@NCFs (171 mV), N-PVP@NCFs (133 mV) and N-*o*-phen@NCFs (139 mV) at a current density of 10 mA/cm^2. This indicates that $Co_{5.47}N$/VN@NCFs possess remarkable catalytic activity under alkaline conditions. The Tafel slope of $Co_{5.47}N$/VN@NCFs was only 81 mV/dec, superior to $Co_{5.47}N$@NCFs (108 mV/dec), VN@NCFs (121 mV/dec), N-PVP@NCFs (83 mV/dec), N-*o*-phen@NCFs (88 mV/dec), and closer to commercial Pt/C (51 mV/dec), indicating a typical Volmer-Heyrovsky mechanism with a rate-determining step (RDS) for the Volmer step (Fig. 4b). The electrochemically active surface area (ECSA), estimated from the double-layer capacitance (C_{dl}) to understand the intrinsic activity of the materials (Fig. S9 in Supporting information), revealed that the C_{dl} of $Co_{5.47}N$/VN@NCFs (178 mF/cm^2) was higher than those of $Co_{5.47}N$@NCFs (112 mF/cm^2), VN@NCFs (114 mF/cm^2), N-PVP@NCFs (147 mF/cm^2), and N-*o*-phen@NCNs (119 mF/cm^2). This indicates the presence of highly exposed metal active sites in $Co_{5.47}N$/VN@NCFs. The stability of HER was evaluated

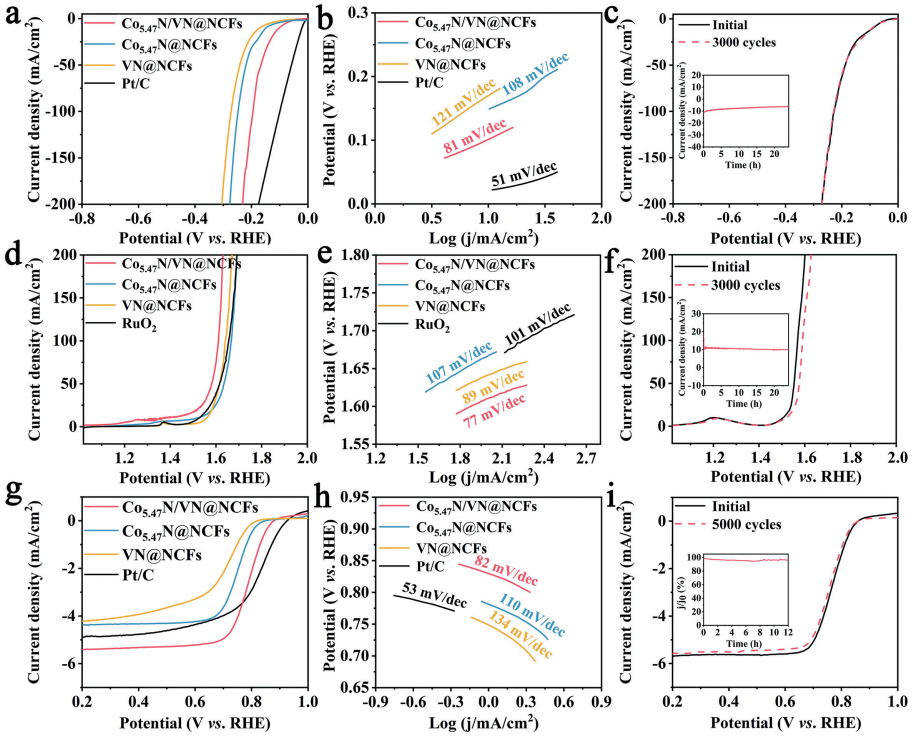

Fig. 4. (a) HER polarization curves and (b) Tafel slopes of different electrocatalysts. (c) 3000 CV cycles and *I-t* curve of $Co_{5.47}N$/VN@NCFs. (d) OER polarization curves and (e) Tafel slopes of different electrocatalysts. (f) 3000 CV cycles and *I-t* curve of $Co_{5.47}N$/VN@NCFs. (g) ORR polarization curves at 1600 rpm and (h) Tafel slopes of different electrocatalysts. (i) 5000 CV cycles and normalized *I-t* curve of $Co_{5.47}N$/VN@NCFs at 0.7 V *versus* RHE. All tests are performed in 0.1 mol/L KOH electrolyte.

through cyclic tests spanning 3000 cycles and current-time (*I-t*) curve (Fig. 4c). $Co_{5.47}N$/VN@NCFs exhibited considerable stability compared to Pt/C, establishing $Co_{5.47}N$/VN@NCFs as a competitive candidate for overall water splitting.

The $Co_{5.47}N$/VN@NCFs demonstrated outstanding OER activity at a current density of 20 mA/cm^2 with a low overpotential of 290 mV in 1 mol/L KOH. This overpotential is significantly lower than that of $Co_{5.47}N$@NCFs (354 mV), VN@NCFs (320 mV), N-PVP@NCFs (299 mV), N-*o*-phen@NCFs (354 mV), and RuO_2 (334 mV) catalysts, and it surpasses other previously reported catalysts (Fig. 4d and Table S5 in Supporting information). This suggests that $Co_{5.47}N$/VN@NCFs can be effectively utilized in rechargeable ZAB and overall water splitting. The Tafel slope of $Co_{5.47}N$/VN@NCFs is 77 mV/dec (Fig. 4e and Fig. S10 in Supporting information), which is lower than that of RuO_2 (101 mV/dec), $Co_{5.47}N$@NCFs (107 mV/dec), VN@NCFs (89 mV/dec), N-PVP@NCFs (99 mV/dec), and N-*o*-phen@NCFs (98 mV/dec). This highlights the exceptional electrocatalytic activity of $Co_{5.47}N$/VN@NCFs, attributed to its abundant active sites for OER and rapid electron/mass transport. Electrochemical impedance spectroscopy (EIS) is depicted in Fig. S11 (Supporting information). $Co_{5.47}N$/VN@NCFs exhibited the smallest charge transport resistance (R_{ct}), indicating fast charge transport kinetics during the OER process. Additionally, the C_{dl}, determined by the ECSA, was found to be higher for $Co_{5.47}N$/VN@NCFs (108 mF/cm^2) compared to $Co_{5.47}N$@NCFs (43 mF/cm^2), VN@NCFs (93 mF/cm^2), N-PVP@NCFs (54 mF/cm^2), and N-*o*-phen@NCFs (87 mF/cm^2) (Fig. S12 in Supporting information). Long-term durability was assessed through cyclic tests spanning 3000 cycles and *I-t* curve, revealing no discernible changes in the polarization curves (Fig. 4f). This highlights its high corrosion resistance in alkaline solutions.

To evaluate the ORR activity of the material, CV tests were conducted in a 0.1 mol/L O_2-saturated KOH solution. A distinct oxygen response peak, typically near 0.75 V, was observed, indicating significant ORR activity (Fig. S13 in Supporting information). The catalytic activity of ORR was initially assessed by linear scanning voltammetry (LSV) using a rotating disk electrode (RDE) at 1600 rpm. The $Co_{5.47}N$/VN@NCFs catalyst exhibited excellent ORR activity with onset potential (E_{onset}) and $E_{1/2}$ of 0.90 and 0.79 V, respectively. These values are comparable to the benchmark Pt/C ($E_{onset} = 0.96$ V, $E_{onset} = 0.83$ V) and better than VN@NCFs ($E_{onset} = 0.83$ V, $E_{1/2} = 0.73$ V), $Co_{5.47}N$@NCFs ($E_{onset} = 0.86$ V, $E_{1/2} = 0.75$ V), N-PVP@NCFs ($E_{onset} = 0.87$ V, $E_{1/2} = 0.76$ V), and N-*o*-phen@NCFs ($E_{onset} = 0.87$ V, $E_{1/2} = 0.77$ V) (Fig. 4g). By introducing VN, $Co_{5.47}N$@NCFs have successfully increased the active sites for the ORR, enhancing the catalytic activity. VN plays a crucial role in the heterojunction, synergistically with $Co_{5.47}N$ to create a electrocatalytic environment more conducive to ORR. More importantly, the Tafel slopes of $Co_{5.47}N$/VN@NCFs were notably small (82 mV/dec), closely resembling those Pt/C (53 mV/dec) and surpass those of $Co_{5.47}N$@NCFs (110 mV/dec), VN@NCFs (134 mV/dec), N-PVP@NCFs (98 mV/dec), and N-*o*-phen@NCFs (95 mV/dec) (Fig. 4h and Fig. S14 in Supporting information). This indicates that with the integration of VN, $Co_{5.47}N$/VN@NCFs displays faster kinetics in the ORR compared to other materials. Additionally, the four-electron transfer number of $Co_{5.47}N$/VN@NCFs, close to Pt/C, was determined based on the LSV curves at different rotational speeds and the Koutechky-Levich (K-L) equation (Fig. S15 in Supporting information). A 12 h durability test was conducted to assess the practical application of $Co_{5.47}N$/VN@NCFs *via* normalized *I-t* curve. Remarkably, the $Co_{5.47}N$/VN@NCFs exhibited only a 5.1% lose (Fig. 4i), which is significantly better than the commercial Pt/C (9.5%) (Fig. S16 in Supporting information). Furthermore, the $Co_{5.47}N$/VN@NCFs showed a negligible loss of 7 mV after consecutive 5000 cycles in O_2-saturated 0.1 mol/L KOH. The outstanding stability of $Co_{5.47}N$/VN@CNFs is attributed to the large specific surface area of the carbon nanofibers, which protects the metal particles from corrosion and aggregation during the ORR process.

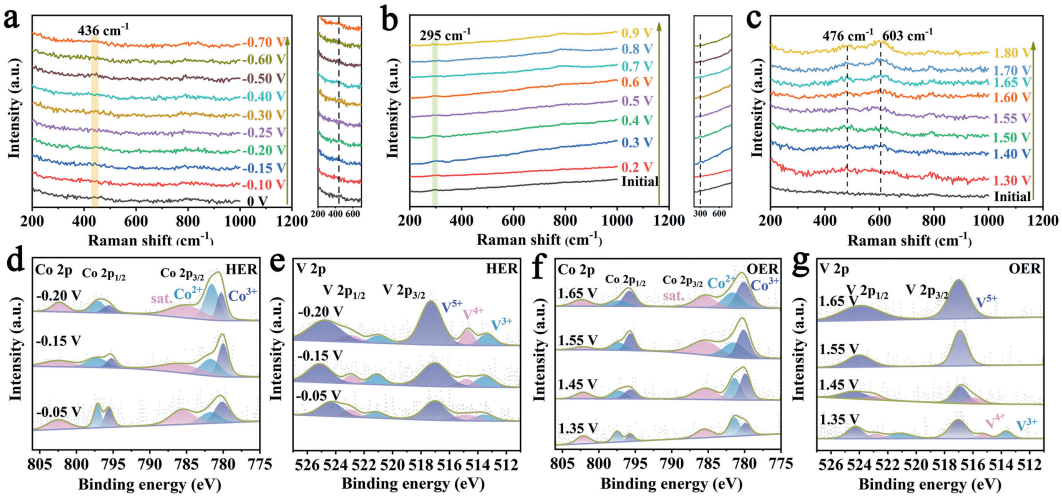

Fig. 5. Operando Raman spectra of $Co_{5.47}N$/VN@NCFs catalyst at different potentials for (a) HER, (b) ORR, and (c) OER process. *Quasi*-operando XPS spectra of $Co_{5.47}N$/VN@NCFs at different potentials, where (d-g) represent the variations in the Co 2p and V 2p spectra during the HER and OER processes.

Therefore, $Co_{5.47}N$/VN@CNFs show great potential for practical applications in ORR. In general, VN regulates the electronic structure of $Co_{5.47}N$@NCFs and significantly increases the number of active sites for HER, OER, and ORR, thereby promoting the progress of these reactions.

The surface species during the catalytic reaction were monitored using operando Raman spectroscopy. The region between 200 cm^{-1} and 1000 cm^{-1} corresponds to lattice vibrations. For the HER, no characteristic peaks were observed at 0 V when the electrode was immersed in a KOH solution. With the increase in external pressure, the intensity of the peak located at 436 cm^{-1} gradually increased, leading to a higher local concentration of OH^-, and subsequently, an increase in the Co-OH intensity during the HER process (Fig. 5a). Regarding the ORR, the peak appearing at 295 cm^{-1} is attributed to CoN, indicating that the active species is primarily the heterojunction itself during the ORR reaction (Fig. 5b). However, with the gradual increase in voltage, this peak decreases again. When the applied voltage is less than 1.5 V, no peak appears, indicating that OER is not occurring. As the applied potential rises from 1.5 V to 1.8 V, a new peak emerges at 476 cm^{-1}, which is close to the A_{2u} vibration peak of β-$Co(OH)_2$, suggesting the formation of β-$Co(OH)_2$. Additionally, an A_{1g} peak appears at 603 cm^{-1}, attributed to the formation of CoOOH intermediates in an alkaline environment. It is noteworthy that the increased peak intensity of CoOOH intermediates is greater than that of β-$Co(OH)_2$, possibly due to the partial conversion of β-$Co(OH)_2$ into CoOOH intermediates (Fig. 5c) [62]. Furthermore, the formation of intermediates at 1.5 V may result in a lower overpotential for the $Co_{5.47}N$/VN redox reaction. Therefore, the conversion of some $Co_{5.47}N$ sites into active CoOOH species could effectively induce OER while preventing the degradation of $Co_{5.47}N$/VN@NCFs catalysts. *Quasi*-operando XPS analysis was employed to investigate the changes in oxidation states during the reaction processes. As depicted in Fig. 5d, the introduction of VN intensified electron transfer at the $Co_{5.47}N$/VN interface, resulting in alterations in the oxidation states of Co and V. With the increase in reduction potential, V^{5+} in V 2p increased, indicating a tendency for V to lose more electrons to Co and shift towards higher binding energy. For Co 2p, more electrons from V were obtained, causing a gradual decrease in the proportion of Co^{3+} and an increase in the proportion of Co^{2+}. Simultaneously, this induced a higher binding energy shift in Co 2p, suggesting that the remaining electrons were more favorable for electron transfer to the surface, promoting reduction reactions (Fig. 5e). This led to the formation of a series of intermediate states in Co, facilitating the creation of multifunctional sites. During the oxidation process, due to electron transfer and the generation of an intrinsic electric field, V^{5+} gradually increased in the V 2p spectrum, inducing the tendency to form more favorable high-valence state Co^{3+} in the Co 2p spectrum (Figs. 5f and g).

Exploiting the trifunctional catalytic capabilities of $Co_{5.47}N$/VN@NCFs for the HER, OER, and ORR, we assessed their potential in practical application through the construction of an overall water splitting device and ZABs. In the two-electrode system for the water splitting setup, $Co_{5.47}N$/VN@NCFs served as both the anode and cathode (Fig. S17a in Supporting information). Impressively, the $Co_{5.47}N$/VN@NCFs‖$Co_{5.47}N$/VN@NCFs cell required only 1.53 V to achieve a current density of 10 mA/cm^2. Notably, the current density of $Co_{5.47}N$/VN@NCFs maintained excellent overall water splitting activity (92%) with no discernible decay over 24 h, surpassing the performance of a Pt/C&RuO_2 cell (57%) (Fig. S17b in Supporting information). Remarkably, the overall water splitting voltage of $Co_{5.47}N$/VN@NCFs in this study was remarkable compared to most reported trifunctional electrocatalysts that do not employ precious metals. The generation of H_2 and O_2 bubbles on the cathode and anode surfaces was monitored separately. Images were captured at 10-min intervals, and volume-time curves were generated after six recordings (Fig. S17c in Supporting information). As depicted in Fig. S17d (Supporting information), the volume-time curve revealed a volume ratio of H_2 to O_2 produced to be 2.03:1, which closely matches the theoretical value of 2:1. Furthermore, the Faraday efficiencies of the generated H_2 and O_2 gases were determined to be 95.7% and 94.4%, respectively, at a current density of 15 mA/cm^2, demonstrating their proximity to 100%. This underscores the effectiveness of $Co_{5.47}N$/VN@NCFs in practical applications.

Given the impressive ORR and OER activities exhibited by $Co_{5.47}N$/VN@NCFs, we assembled liquid rechargeable ZABs using $Co_{5.47}N$/VN@NCFs as the cathode and zinc plates as the anode (Fig. 6a). For comparison, a mixture of Pt/C and IrO_2 with a 1:1 mass ratio was also incorporated into the batteries. As depicted in Fig. 6b, the open-circuit voltage (OCV) was determined to be 1.446 V, and it remained stable over an extended period. The rechargeable ZAB, equipped with $Co_{5.47}N$/VN@NCFs, demonstrated a high discharge specific capacity of 789 mAh/g, outperforming Pt/C&RuO_2 (710 mAh/g) at a current density of 10 mA/cm^2, considering the mass of consumed zinc (Fig. 6c). The ZAB with $Co_{5.47}N$/VN@NCFs achieved an ultra-high power density of 207 mW/cm^2 at a current density of 249.7 mA/cm^2, sur-

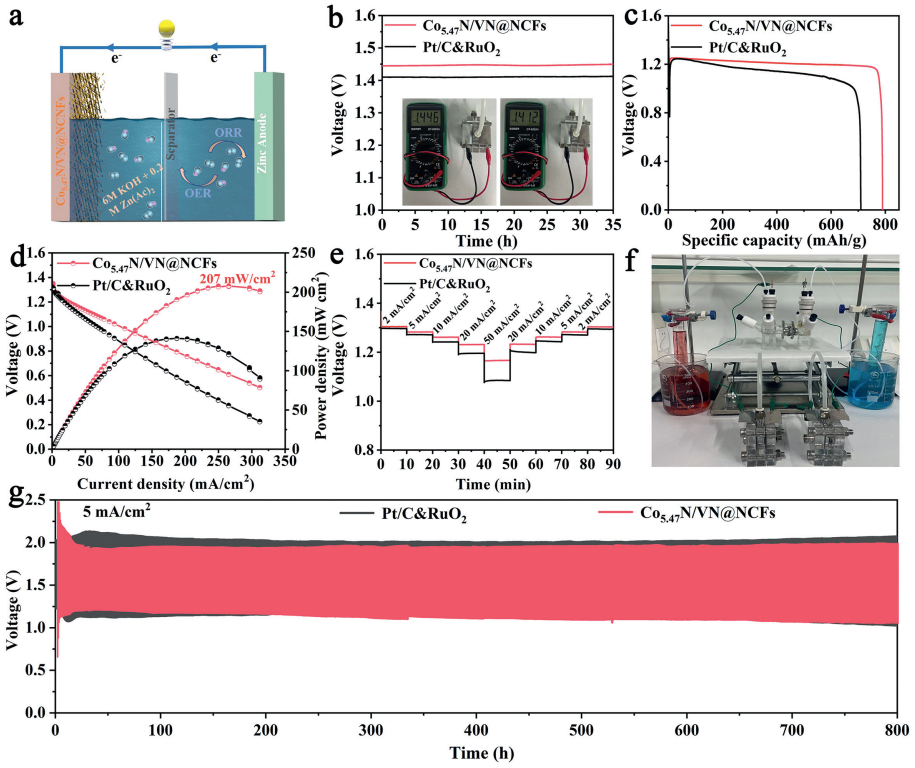

Fig. 6. (a) Schematic illustration of ZAB. (b) OCV of ZAB assembled with $Co_{5.47}N/VN@NCFs$ and $Pt/C\&RuO_2$ (Inset: digital photo of open circuit voltage obtained by multimeter). (c) Discharged specific capacity curves at 10 mA/cm^2. (d) Power density curves, (e) discharged curves at various current densities of the assembled ZABs. (f) Digital photo of the water splitting system powered by two serial ZABs and (g) discharged-charged curves of ZAB assembled with $Co_{5.47}N/VN@NCFs$ and $Pt/C\&RuO_2$ at 5 mA/cm^2.

passing the 140 mW/cm^2 of the ZAB assembled with $Pt/C\&RuO_2$ at a current density of 202.8 mA/cm^2. This confirms the excellent catalytic performance under practical conditions (Fig. 6d and Table S6 in Supporting information). Remarkably, the discharge tests for both air batteries showed minimal voltage fluctuations over a current density range of 2 mA/cm^2 to 50 mA/cm^2, as displayed in Fig. 6e, underscoring their reversibility and stable performance. Fig. 6f demonstrates that two ZABs, each equipped with $Co_{5.47}N/VN@NCFs$, connected in series can power the overall water splitting device composed of two identical electrodes. The change in the volume of H_2 and O_2 collected in the cylinder over time clearly demonstrates the practical application of integrating these two devices (Fig. S18 in Supporting information). To assess the durability of the ZAB with $Co_{5.47}N/VN@NCFs$, a discharge/charge cycle test was conducted at a constant current of 5 mA/cm^2. The voltage difference of 0.94 V for $Co_{5.47}N/VN@NCFs$ ZAB was lower than that of 1.03 V for $Pt/C\&RuO_2$ after 800 h of cycling (Fig. 6g). It can also perform stably for more than 600 h at 10 mA/cm^2, further indicating the well durability (Fig. S19 in Supporting information). This work lays the foundation for the development of efficient Co/V-based heterojunction multifunctional electrocatalysts for renewable energy technologies.

DFT calculations are additionally utilized to probe into reaction mechanism. The adsorption Gibbs free energy (ΔG_{H^*}) of H* species on the active sites of VN, $Co_{5.47}N$, and $Co_{5.47}N/VN$ surfaces are shown in Fig. 7a and Figs. S20-S24 (Supporting information). The ΔG_{H^*} values for the Co1 and Co2 sites of $Co_{5.47}N$ are −0.561 and −0.699 eV, respectively (Table S7 in Supporting information). This indicates a strong interaction between H* species and these sites, making the desorption of H* and the formation of H_2 relatively challenging. Conversely, on the VN surface, the interaction is relatively weak, making it challenging for them to form stable adsorption structures. The preceding theoretical and experimental results indicate that VN can alter the diversity of the valence states of Co sites in $Co_{5.47}N$, thereby exerting a significant impact on the HER performance. The ΔG_{H^*} values for Co1, Co2, and Co3 sites of $Co_{5.47}N/VN$ are –0.182, –0.031, and 0.401 eV, respectively, consistent with the results of Bader charge analysis. Additionally, VN can increase HER active sites. On the surfaces of VN and $Co_{5.47}N$, the adsorption of N sites and H* is strong (–1.883 and –1.197 eV), making them less favorable as HER active sites. However, with the interface interaction between VN and $Co_{5.47}N$, the electronic structure of the N sites at the $VN/Co_{5.47}N$ interface undergoes corresponding changes. This results in a transformation of the ΔG_{H^*} for H* species on N1 and N2 sites to −0.303 eV and −0.249 eV. The above calculations confirm the electronic modulation effect of VN on $Co_{5.47}N$, activating the HER activity of Co and N sites and making ΔG_{H^*} more consistent with the Sabatier principle, in accordance with the analysis results of ELF.

Under alkaline conditions, the catalytic performance of the catalyst in the OER is linked to intermediates (OOH*, O*, and OH*) and their adsorption/desorption characteristics (Eqs. S8-S11 in Supporting information). On the $Co_{5.47}N$ surface, O* exhibits a stronger adsorption at Co1 and Co2 sites, while the adsorption strength of OOH* is relatively weaker. Therefore, the formation of OOH* is the RDS with overpotential of 2.516 V and 2.582 V, respectively (Fig. 7b and Figs. S25-S30 in Supporting information). For the V sites on the VN surface, the transformation of O* to OOH* is also the RDS. However, the interaction between OOH* and V sites is strengthened, resulting in a reduction of the overpotential to 2.275 V (Table S8 in Supporting information). It can be anticipated that after the introduction of VN, the interface interactions will redistribute the spatial charge density in $VN/Co_{5.47}N$. This alteration is expected to modify the adsorption characteristics of active sites for oxygen-containing intermediates, potentially improving the catalytic OER

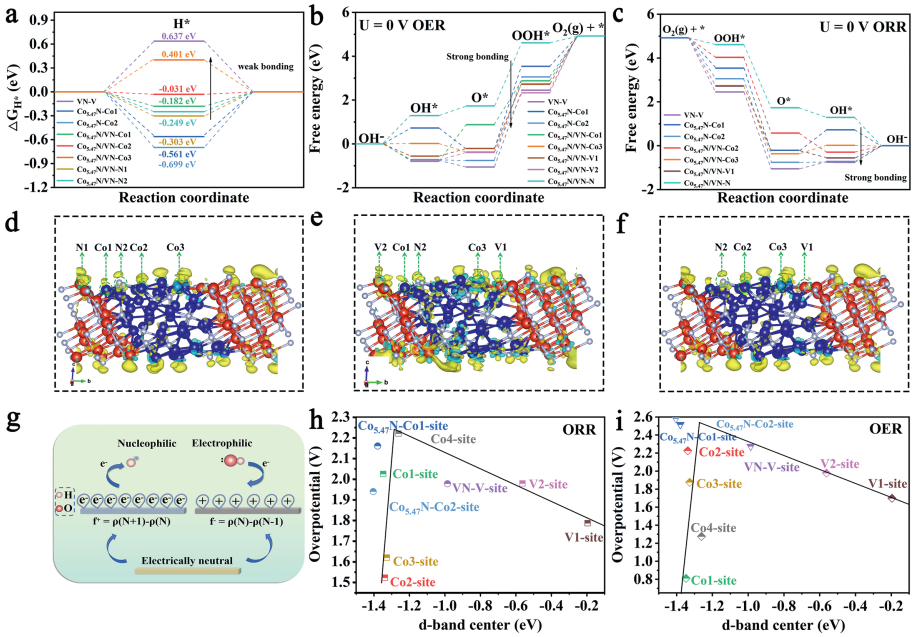

Fig. 7. (a) Free energy diagrams for HER. (b) Free energy diagrams for OER at $U = 0$ V. (c) Free energy diagram for ORR at $U = 0$ V. (d) The nucleophilic fukui function of $Co_{5.47}N/VN$ during HER. (e) The electrophilic fukui function of $Co_{5.47}N/VN$ during OER. (f) The nucleophilic fukui function of $Co_{5.47}N/VN$ during ORR. (g) The fukui function mechanism diagram. (h, i) d-band center and overpotential relationship for ORR and OER. The labels in (d-f) represent the active sites with promising performance.

activity. The OER activity of the Co1, Co2, Co3, and Co4 sites at the $Co_{5.47}N/VN$ heterojunction interface has been improved to varying degrees. Although the RDS at the Co3 site remains unchanged, the enhanced adsorption of OOH* at this site leads to a reduced overpotential to 1.876 V. For the Co1 and Co4 sites, the adsorption of O species on their surfaces significantly decreases, while the adsorption of OOH* markedly increases. This can lead to a shift in the RDS and bring about a substantial improvement in overpotential (0.811 V and 1.276 V). Thus, VN can indeed effectively alter the adsorption characteristics of active sites in $Co_{5.47}N$, contributing to the enhancement of OER activity of the catalyst. In addition, the interface electron transfer also alters the electronic structure of V sites and adsorption characteristics for O radicals. These results in a decrease in overpotential of 0.576 V and 0.297 V at the V1 and V2 sites, respectively, compared to V sites on pure VN surface. This feedback can help activate the OER activity of V sites and also reflect the synergistic catalytic role of Co and V sites at the interface. The OER process involves N sites easily coordinating with transition metals to form negatively charged ions, leading to unfavorable adsorption of OH^- at those sites in terms of energy. The adsorption process of oxygen-containing species on the N sites of VN and $Co_{5.47}N$ surfaces tend to preferentially bind to transition metals, thus forming stable adsorption configurations (Fig. S31 in Supporting information). Thus, N sites are challenging to serve as catalytic active sites. However, in the $Co_{5.47}N/VN$ heterojunction, significant changes in adsorption properties of O*, OH*, and OOH* occur at the N1 site, driven by alterations in the interface space charge, showcasing distinctive catalytic behavior. The overpotential at this site is 1.648 V. The above computational results indicate that VN enhances the adsorption properties of Co sites for OOH* species and improves the adsorption of O* species at nearby V sites in the $Co_{5.47}N/VN$ heterojunction. This compensatory effect facilitates collaborative elementary reactions, enhancing the overall catalyst activity.

The metal active sites on $Co_{5.47}N$ and VN surfaces exhibit different catalytic activities in ORR (Fig. 7c). The Co1 site on the $Co_{5.47}N$ surface shows a weak interaction with OH*, and the reaction of O* with H_2O to generate OH* is the RDS, with a theoretical overpotential of 2.164 V (Figs. S32 and S33, Table S9 in Supporting information). In contrast, the Co2 site on the $Co_{5.47}N$ surface and the V site on the VN surface show strong interaction with OH*, and the generation of OH^- becomes the RDS, resulting in theoretical overpotential of 1.943 V and 1.981 V, respectively. Therefore, adapting the electronic structure of active sites is crucial for enhancing ORR activity, allowing effective coordination of the four elementary reactions and boosting overall activity. The introduction of VN further modifies the adsorption characteristics of OH* at the heterojunction interface, leading to varied overpotential for ORR at different active sites. In comparison to the Co1 site in $Co_{5.47}N$, the introduction of VN enhances the adsorption energy of OH* at the Co2, Co3, and V sites at the heterojunction interface to different extents. Conversely, in comparison to the Co2 site in $Co_{5.47}N$ and the V site on the VN surface, the introduction of VN weakens the adsorption energy of OH* at the Co2, Co3, and V sites at the heterojunction interface to varying degrees. This compromise effect results in a reduction of the theoretical overpotential at the Co2, Co3, and V1 sites to 1.522, 1.619, and 1.786 V, respectively. Additionally, N2 sites also exhibit excellent ORR activity at the heterojunction interface. All four elementary reactions at this site are thermodynamically spontaneous processes, with the first elementary reaction being the RDS, and the theoretical overpotential for ORR is only 0.919 V. The above results clearly indicate that the introduction of VN significantly influences the electronic structure of active sites at the interface, increasing the differences in the valence states between active sites (Table S10 in Supporting information). This ultimately endows Co1, Co3, V1, V2, and N sites with excellent OER activity, while Co2, Co3, V1, and N sites exhibit remarkable ORR activity. The diversity of catalytic active sites and their complementary characteristics enable the $Co_{5.47}N/VN$ catalyst to simultaneously demonstrate excellent HER/ORR and OER synergistic catalytic activity.

To further validate the reaction characteristics and diversity of catalytic sites, Figs. 7d–f and Figs. S34-S36 (Supporting information) illustrate the electrophilicity ($f^- = \rho(N)$ - $\rho(N\text{-}1)$) and nucleophilicity fukui functions ($f^+ = \rho(N+1)$ - $\rho(N)$) of the $Co_{5.47}N$, VN, and $Co_{5.47}N/VN$ [63,64]. For $Co_{5.47}N$ and VN, both f^- and f^+ are

mainly on the metal sites (V and Co), suggesting a single catalytic activity for various reaction intermediates like HER, OER, and ORR (Fig. S37 in Supporting information). It is challenging for these catalysts to simultaneously exhibit optimal adsorption, activation, reaction, and desorption properties for different reaction intermediates, significantly limiting their multifunctional catalytic activity. In contrast, the surface active sites of the $Co_{5.47}N$/VN heterojunction display distinctly shaped electrophilicity and nucleophilicity fukui functions, consistent with Bader charge analysis results. This further confirms the diversity and multifunctionality of the surface active sites of the $Co_{5.47}N$/VN catalyst (Fig. 7g). Catalytic sites with pronounced f^+ distributions on the nucleophilic fukui function surface, such as Co1, Co2, Co3, N1, and N2, tend to preferentially interact with H^+, thereby demonstrating significantly enhanced HER activity. Similarly, for Co2, Co3, V1, and N2, they tend to bind with oxygen-containing intermediate species, exhibiting excellent ORR activity. The electrophilic fukui function f^- on the surface of the $Co_{5.47}N$/VN catalyst also shows significant variability, with sites like Co1, Co3, Co4, N2, and V1 displaying noticeable electrophilic activity. These sites are more likely to act as electron acceptors, interacting with relevant oxygen-containing species and facilitating the transfer of electrons from the adsorbed species to the catalyst surface, ultimately enhancing the OER activity of the catalyst. Furthermore, the above results also indicate that the Co2, Co3, and N2 sites exhibit tri-functional catalytic activity, which is absent in catalysts with a single active site (*i.e.*, VN or $Co_{5.47}N$). This further demonstrates the electronic modulation of VN on $Co_{5.47}N$ in the heterojunctions.

Figs. 7h and i present the relationship between the theoretical overpotential for the OER and ORR processes and the d-band center of adsorption-active sites. The computational results indicate a well-defined volcano correlation between different catalytic active sites and the theoretical overpotential, whether in the OER or ORR process. This suggests that the introduction of VN leads to significant diversity in the electronic structure properties, such as oxidation state and d-band center, of catalytic sites at the heterojunction interface. It enables better adaptability and synergistic effects in the adsorption, reaction, and desorption of intermediate species during HER, OER, and ORR processes. This diversity and synergy are crucial factors contributing to the excellent tri-functional electrocatalytic activity of $Co_{5.47}N$/VN. The obtained research results will lay a crucial foundation for manipulating the diversity of catalytic active sites through stoichiometry and interface interactions to enhance the multifunctional electrocatalytic properties of catalysts.

In conclusion, $Co_{5.47}N$ exhibits diverse valence states and a high-density d-electron state at the Co site, benefiting trifunctional electrocatalytic activity. The introduced VN could regulate the electronic structure of $Co_{5.47}N$, thus improving the adsorption and electrocatalytic activity of intermediates. Based on computational results, $Co_{5.47}N$/VN@NCFs catalyst has been constructed, which performs excellent performance in HER, OER and ORR. Two series-connected assembled ZABs can drive overall water splitting. Quasi-operando XPS analyses clarify that electron regulation of VN effects the valence state of Co. Additionally, the VN with enriched active sites promotes the tri-functional electrocatalytic activity. This study aims to lay a crucial foundation for simultaneously regulating the diversity and functionality of catalytic active sites.

Declaration of competing interest

The authors declare that they have no known competing financial interests or personal relationships that could have appeared to influence the work reported in this paper.

CRediT authorship contribution statement

Xinxin Zhang: Data curation, Formal analysis, Investigation, Writing – original draft, Writing – review & editing. **Zhijian Liang:** Data curation, Formal analysis, Investigation, Methodology. **Xu Zhang:** Data curation, Investigation, Methodology. **Qian Guo:** Investigation, Methodology. **Ying Xie:** Data curation, Methodology, Software, Writing – original draft, Writing – review & editing. **Lei Wang:** Data curation, Investigation, Project administration, Writing – original draft, Writing – review & editing. **Honggang Fu:** Conceptualization, Project administration, Resources, Writing – original draft, Writing – review & editing.

Acknowledgments

We gratefully acknowledge the support of this research by the National Key R&D Program of China (No. 2023YFA1507204), the National Natural Science Foundation of China (Nos. U20A20250, 22279030, 22179034), the Natural Science Foundation of Heilongjiang Province (No. ZD2023B002).

Supplementary materials

Supplementary material associated with this article can be found, in the online version, at doi:10.1016/j.cclet.2024.109935.

References

[1] F. Kong, X. Fan, A. Kong, et al., Adv. Funct. Mater. 28 (2018) 1803973.
[2] Z.Q. Zhang, Y. Lei, W.M. Huang, Chin. Chem. Lett. 33 (2022) 3623–3631.
[3] H. Liu, J. Guan, S. Yang, et al., Adv. Mater. 32 (2020) 2003649.
[4] H. Huang, A. Huang, D. Liu, et al., Adv. Mater. 35 (2023) 2303109.
[5] L. Wang, Z. Xu, C.H. Kuo, et al., Angew. Chem. Int. Ed. 62 (2023) e202311937.
[6] C.H. Niu, Y.X. Zhang, J. Dong, et al., Chin. Chem. Lett. 32 (2021) 2484–2488.
[7] J.J. Li, S.B. Zou, J.Z. Huang, et al., Chin. Chem. Lett. 34 (2023) 107222.
[8] J. Song, Y. Chen, H. Huang, et al., Adv. Sci. 9 (2022) 2104522.
[9] L. Deng, S.F. Hung, Z.Y. Lin, et al., Adv. Mater. 35 (2023) 2305939.
[10] Y. Hao, S.F. Hung, W.J. Zeng, et al., J. Am. Chem. Soc. 145 (2023) 23659–23669.
[11] Q. Qin, H. Jang, P. Li, et al., Adv. Energy Mater. 9 (2018) 1803312.
[12] Y. Pan, S. Liu, K. Sun, et al., Angew. Chem. Int. Ed. 57 (2018) 8614–8618.
[13] J. Balamurugan, T.T. Nguyen, D.H. Kim, N.H. Kim, J.H. Lee, Appl. Catal. B: Environ. 286 (2021) 119909.
[14] S.H. Chae, A. Muthurasu, T. Kim, et al., Appl. Catal. B: Environ. 293 (2021) 120209.
[15] L. Fang, S. Seifert, R.E. Winans, T. Li, Small Methods 5 (2021) 2001194.
[16] S. Jiao, X. Fu, H. Huang, Adv. Funct. Mater. 32 (2021) 2107651.
[17] A. Nairan, P. Zou, C. Liang, et al., Adv. Funct. Mater. 29 (2019) 1903747.
[18] B. Liu, B. He, H.Q. Peng, et al., Adv. Sci. 5 (2018) 1800406.
[19] S. Ye, F. Luo, Q. Zhang, et al., Energy Environ. Sci. 12 (2019) 1000–1007.
[20] Z. Li, Z. Tian, H. Cheng, et al., Energy Storage Mater. 59 (2023) 102764.
[21] Y. Chen, X. Zheng, J. Cai, et al., ACS Catal. 12 (2022) 7406–7414.
[22] H. Zhang, W. Xia, H. Shen, et al., Angew. Chem. Int. Ed. 132 (2019) 1871–1877.
[23] H. Wang, T. Zhai, Y. Wu, et al., Adv. Sci. 10 (2023) 2301706.
[24] H. Jia, N. Yao, C. Yu, H. Cong, W. Luo, Angew. Chem. Int. Ed. 135 (2023) e202313886.
[25] J. Zhu, J. Qian, X. Peng, B. Xia, D. Gao, Nanomicro Lett. 15 (2023) 30.
[26] C. Zhong, J. Zhang, L. Zhang, et al., ACS Energy Lett. 8 (2023) 1455–1462.
[27] C. Huang, B. Zhang, Y. Wu, et al., Appl. Catal. B: Environ. 297 (2021) 120461.
[28] D. Zhao, Z. Cui, S. Wang, J. Qin, M. Cao, J. Mater. Chem. A 4 (2016) 7914–7923.
[29] L. Dai, F. Yao, L. Yu, et al., Adv. Energy Mater. 12 (2022) 2200974.
[30] W. Luo, Y. Yu, Y. Wu, et al., Appl. Catal. B: Environ. 336 (2023) 2008511.
[31] D. Guo, Z. Wan, Y. Li, B. Xi, C. Wang, Adv. Funct. Mater. 31 (2020) 2008511.
[32] X. Wu, G. Han, H. Wen, et al., Energy Environ. Mater. 5 (2021) 935–943.
[33] J. Zheng, A. Xu, A. Wu, X. Li, ACS Appl. Mater. Interfaces 13 (2021) 21231–21240.
[34] Z. Wu, Y. Zhao, W. Xiao, et al., ACS Nano 16 (2022) 18038–18047.
[35] T. Wang, X. Cao, H. Qin, et al., J. Mater. Chem. A 9 (2021) 21094–21100.
[36] M. Jiang, C. Fu, R. Cheng, et al., Adv. Sci. 7 (2020) 2000747.
[37] Y. Hu, Z. Huang, Q. Zhang, et al., J. Colloid Interface Sci. 643 (2023) 455–464.
[38] Y. Zhou, Z. Zhou, R. Shen, et al., Energy Storage Mater. 13 (2018) 189–198.
[39] W. Qi, H. Wang, J. Liu, et al., Mater. Chem. Front. 7 (2023) 607–627.
[40] J. Song, D. Yu, X. Wu, et al., Chem. Eng. J. 437 (2022) 135281.
[41] N. Wang, B. Hao, H. Chen, et al., Chem. Eng. J. 413 (2021) 127954.
[42] X. Shu, S. Chen, S. Chen, W. Pan, J. Zhang, Carbon 157 (2020) 234–243.
[43] Y. Yang, R. Zeng, Y. Xiong, F.J. DiSalvo, H.D. Abruna, J. Am. Chem. Soc. 141 (2019) 19241–19245.
[44] T. Liu, S. Cai, G. Zhao, et al., J. Energy Chem. 62 (2021) 440–450.
[45] W. Yuan, S. Wang, Y. Ma, et al., ACS Energy Lett. 5 (2020) 692–700.

[46] D. Guo, Z. Zeng, Z. Wan, et al., Adv. Funct. Mater. 31 (2021) 2101324.
[47] H. Yu, S. Zhu, Y. Hao, et al., Adv. Funct. Mater. 33 (2023) 2212811.
[48] R. Zhang, Z. Wei, G. Ye, et al., Adv. Energy Mater. 11 (2021) 2101758.
[49] J. Luo, X. Tian, J. Zeng, et al., ACS Catal. 6 (2016) 6165–6174.
[50] D. He, L. Cao, J. Huang, et al., Chem. Eng. J. 429 (2022) 2101758.
[51] G. Zhou, G. Liu, X. Liu, et al., Adv. Funct. Mater. 32 (2021) 6165–6174.
[52] X. Zhang, P. Yu, G. Xing, et al., Small 18 (2022) 2205228.
[53] Y. Pan, X. Ma, M. Wang, et al., Adv. Mater. 34 (2022) 2203621.
[54] J. Leverett, R. Daiyan, L. Gong, et al., ACS Nano 15 (2021) 12006–12018.
[55] T.T. Nguyen, J. Balamurugan, H.W. Go, et al., Chem. Eng. J. 427 (2022) 131774.
[56] W. Jiang, J. Chen, G. Qian, et al., Electrochim. Acta 390 (2021) 138887.
[57] C. Huang, D. Wu, P. Qin, et al., Nano Energy 73 (2020) 104788.
[58] C. Pi, Z. Zhao, X. Zhang, et al., Chem. Eng. J. 416 (2021) 129130.
[59] G. Zhang, X. Liu, P. Yu, et al., Chin. Chem. Lett. 33 (2022) 3903–3908.
[60] M. Tong, F. Sun, Y. Xie, et al., Angew. Chem. Int. Ed. 60 (2021) 14005–14012.
[61] Z. Rong, C. Dong, S. Zhang, W. Dong, F. Huang, Nanoscale 12 (2020) 6089–6095.
[62] K. Ding, J. Hu, J. Luo, et al., Adv. Funct. Mater. 32 (2022) 2207331.
[63] M.L. Ceron, T. Gomez, M. Calatayud, C. Cardenas, J. Phys. Chem. A 124 (2020) 2826–2833.
[64] S. Gusarov, S.R. Stoyanov, S. Siahrostami, J. Phys. Chem. C 124 (2020) 10079–10084.